RSC Medicinal Chemistry

ROYAL SOCIETY OF CHEMISTRY

RESEARCH ARTICLE

View Article Online
View Journal

Cite this: DOI: 10.1039/c9md00537d

Computer-aided discovery of phenylpyrazole based amides as potent S6K1 inhibitors†

Yan Yin, *[a] Yuxing Sun,[a] Lianhua Zhao,[a] Jinpeng Pan[a] and Yangbo Feng[bc]

Received 15th November 2019,
Accepted 4th April 2020

DOI: 10.1039/c9md00537d

rsc.li/medchem

Ribosomal protein S6 kinase beta-1 (S6K1) is an attractive therapeutic target. In this study, computational analysis of five thiophene urea-based S6K1 inhibitors was performed. Molecular docking showed that the five compounds formed hydrogen bonds with residues Glu173 and Leu175 of S6K1 and hydrophobic interactions with residues Val105, Leu97 and Met225, and these interactions were key elements for the inhibitory potency of the compounds. Binding free energy (ΔG_{bind}) decomposition analysis showed that Leu97, Glu173, Val 105, Leu175, Leu97 and Met225 contribute the most to ΔG_{bind}. Based on the computer results, phenylpyrazole based amides (**D1–D3**) were designed and synthesized. Biological evaluation revealed that **D2** exhibited 15.9 nM S6K1 inhibition, medium microsomal stability and desirable bioavailability.

Introduction

Ribosomal protein S6 kinase beta-1 (S6K1), also known as p70 S6 kinase-1, is a serine/threonine kinase that contains two non-identical kinase catalytic domains and phosphorylates several proteins. S6K1 activity is suggested to be closely associated with diverse cellular processes, including protein synthesis,[1] mRNA processing,[2] glucose homeostasis,[3] and cell growth and apoptosis.[4] Thus, S6K1 is an attractive therapeutic target to develop drugs that treat aging-related diseases,[5] type 2 diabetes[6] and cancer.[7] Although ATP-competitive small molecular S6K1 inhibitors exist,[8,9] there remains an urgent need to identify new potent S6K1 inhibitors because of increasing pharmacological interest.

The group of Kablaoui has developed a series of potent and selective thiophene urea-templated S6K1 inhibitors (**Compd. 1–5**; Fig. 1). They divided where these compounds interact with S6K1 into three regions, *i.e.*, the hinge region, hydrophobic pocket and solvent exposed region, and provided a possible pharmacophore model.[9] Computational methods can predict affinity before a compound is synthesized and hence accelerate the drug discovery process by reducing the number of iterations required and have often provided novel structures. Recently, our research group designed small bioactive organic molecules by using combined computational studies.[10] There is no computational work or X-ray cocrystal structures to support Kablaoui's hypothesis. Thus, in this study, molecular docking was used to predict the binding modes of Kablaoui's S6K1 inhibitors, and molecular dynamics (MD) simulations of **Compd. 5** followed by calculation of the binding free energy (ΔG_{bind}) with the molecular mechanics-generalized-Born/surface area (MM/GBSA) method were used to gain insight into the origin of the inhibitory activity at the amino acid residue level. Three fluorine-containing S6K1 inhibitors (**D1–D3**) were then designed according to the computational results, and the chemical synthesis and an *in vitro* bioassay test were performed to validate the molecular models. Finally, the pharmacokinetic properties and metabolism stabilities of **D1** and **D2** were investigated.

Results and discussion

As shown in Fig. 1, the replacement of the phenol with a 5-amino indazole increased the inhibitory activity (IC_{50} = 34 nM for **Compd. 3** *vs.* 4 μM for **Compd. 2**). The IC_{50} of **Compd. 1** with the pyridinylphenyl ether was lower than those of the

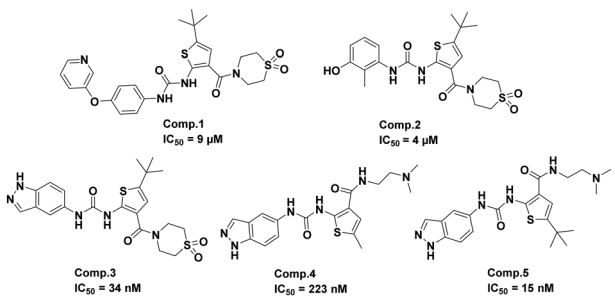

Fig. 1 S6K1 inhibitors reported by Kablaoui's group.

[a] *School of Chemical and Environmental Engineering, Shanghai Institute of Technology, 100 Hai Quan Rd., Shanghai, 201418, P. R. China. E-mail: yinyan@sit.edu.cn*
[b] *Medicinal Chemistry, The Scripps Research Institute, 130 Scripps Way, Jupiter, Florida 33458, USA*
[c] *Reaction Biology Corporation, Malvern, PA 19355, USA*

† Electronic supplementary information (ESI) available. See DOI: 10.1039/c9md00537d

other compounds but still within a measurable range (IC_{50} = 9 μM). Substitutions at the 5-position of the thiophene ring had clear effects on inhibition (IC_{50} = 223 nM for **Compd. 4** with the methyl group *vs.* 15 nM for **Compd. 5** with the *t*-butyl group). Modifications to the amide region located at the 3-position of the thiophene ring only gave a slight change in activity (IC_{50} = 34 nM for **Compd. 3** *vs.* 15 nM for **Compd. 5**). The following SAR explanation was provided by Kablaoui's group:[9] (a) the indazole moiety possibly interacts with the hinge region of the S6K1 binding pocket; (b) the 5-position substituent fits into a hydrophobic pocket of S6K1; (c) the 3-position lacks key interactions with the S6K1 binding pocket and the 3-position of thiophene is a solvated region.

Molecular docking predicts the preferred orientation of a ligand in a protein–ligand complex. Knowledge of the preferred orientation is used to predict the strength of the association or binding affinity of the ligand–protein complexes. **Compd. 1–5** were docked into the binding site of S6K1 (Fig. 2) to understand the pharmacophore models of Kablaoui and guide the potent S6K1 inhibitor design.

In the S6K1–**Compd. 1** complex (Fig. 2a and b), there was one hydrogen bond (H-bond) between Leu175 and the pyridine ring in the hinge binding region, seven hydrophobic interactions (Leu97–phenyl ring, Leu97–pyridine ring, Ala121–pyridine ring, Met225–pyridine ring, and Met225–phenyl ring in the hinge binding region, and Val105–thiophene and Val105–*t*-butyl group in the hydrophobic region), and one unfavorable steric clash between the S atom of Met225 and the O atom of the phenol. In the S6K1–**Compd. 2** complex (Fig. 2c and d), there were two H-bonds in the hinge binding region (Leu175···OH and Met225···phenyl ring) and six hydrophobic interactions (Leu97–phenyl ring, Leu97–methyl group of the phenyl ring, Tyr174–methyl group of the phenyl ring and Leu175–phenyl ring in the hinge binding region and Val105–thiophene and Val105–*t*-butyl group in the hydrophobic region). In the S6K1–**Compd. 3** complex (Fig. 2e and f), there were two H-bonds in the hinge binding region (Glu173–C═O···H–N in the pyrazole ring and Leu175–N–H···N in the pyrazole ring) and nine hydrophobic interactions (Leu97–phenyl ring, Leu97–pyrazole ring, Ala121–phenyl ring, Ala121–pyrazole ring, Leu175–phenyl ring, Leu175–pyrazole ring and Met225–phenyl ring in the hinge binding region and Val105–thiophene and Val105–*t*-butyl group in the hydrophobic region). In the S6K1–**Compd. 4** complex (Fig. 2g and h), there were three H-bonds (Glu173–C═O···H–N in the pyrazole ring and Leu175–N–H···N in the pyrazole ring of the hinge binding region and Glu222–C═O···H–$CHCH_2N(CH_3)_2$ in the solvated region) and eight hydrophobic interactions (Met225–phenyl ring, Leu97–phenyl ring, Ala121–pyrazole ring, Leu175–phenyl ring, Leu17–pyrazole ring and Met225–pyrazole ring in the hinge binding region and Val105–thiophene and Val105–*t*-butyl group in the hydrophobic region). In the S6K1–**Compd. 5** complex (Fig. 2i and j), there were three H-bonds (Glu173–C═O···H–N in the pyrazole ring and Leu175–N–H···N in pyrazole ring in hinge binding region and Glu222–C═O···H–$CHCH_2N(CH_3)_2$

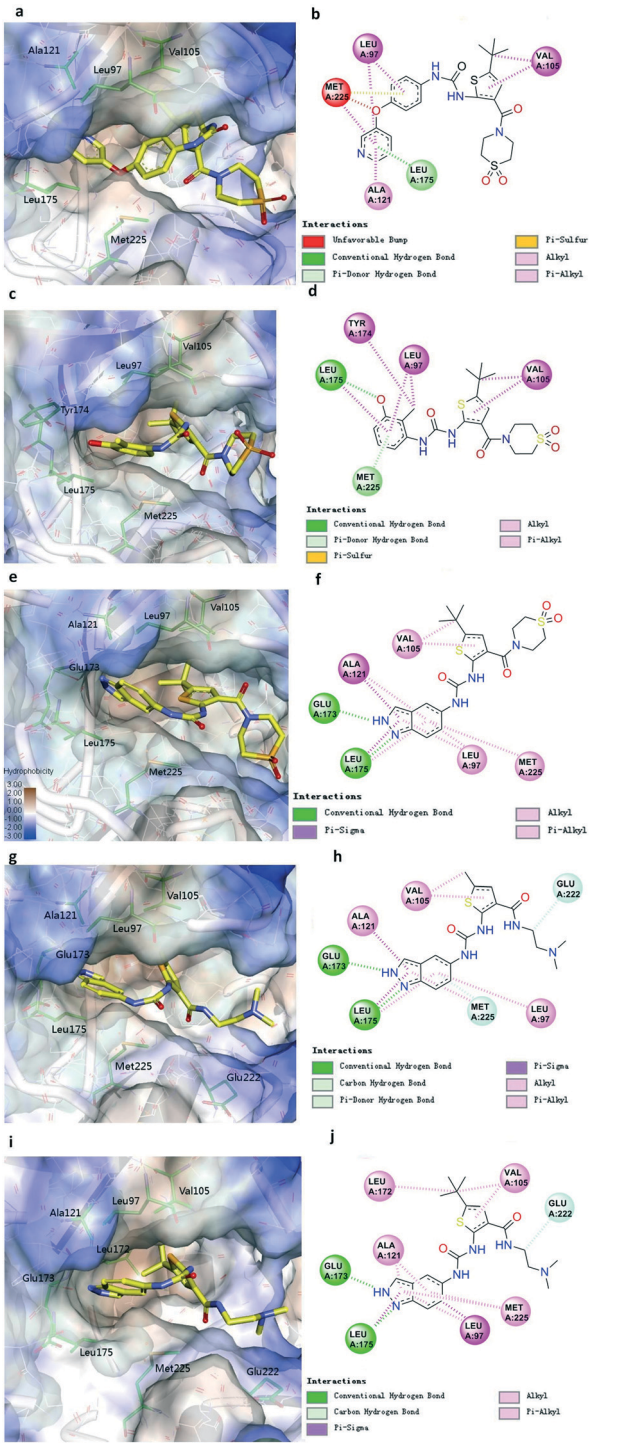

Fig. 2 Docking results. (a) 3D view of the S6K1–**Compd. 1** complex. (b) 2D view of the S6K1–**Compd. 1** complex. (c) 3D view of the S6K1–**Compd. 2** complex. (d) 2D view of the S6K1–**Compd. 2** complex. (e) 3D view of the S6K1–**Compd. 3** complex. (f) 2D view of the S6K1–**Compd. 3** complex. (g) 3D view of the S6K1–**Compd. 4** complex. (h) 2D view of the S6K1–**Compd. 4** complex. (i) 3D view of the S6K1–**Compd. 5** complex. (j) 2D view of the S6K1–**Compd. 5** complex. In the 3D view, carbon atoms of the ligand and protein are shown in yellow and white, respectively. In the 2D view, conventional H-bonds, carbon H-bonds, and pi–donor H-bonds are shown as green dotted lines. Pi–sulfur, alkyl, pi–alkyl and pi–sigma interactions (hydrophobic interactions) are shown as pink dotted lines, except for the pi–sigma interactions, which are colored purple.

in the solvated region) and ten hydrophobic interactions (Leu97–pyrazole ring, Leu97–phenyl ring, Ala121–phenyl ring, Ala121–pyrazole ring, Leu175–pyrazole ring, Met225–phenyl ring and Met225–pyrazole ring in the hinge binding region, Val105–thiophene and Val105–*t*-butyl group in the hydrophobic region, and Leu172–*t*-butyl group in the solvated region).

There were several key binding elements that contributed to the high potency of **Compd. 3–5**. Fig. 2f, h, and j indicate that the pyrazole headgroup binds to the hinge region of S6K1 through H-bonds. The first H-bond is between the NH of Leu175 and the N of the pyrazole ring, and the second H-bond is between the N of Glu173 and the NH of the pyrazole ring. The second H-bond probably accounts for the higher inhibitory activity of **Compd. 3–5** when compared with that of **Compd. 1** and **Compd. 2**, because this H-bond is absent in these two compounds (Fig. 2b and d). Importantly, there is a hydrophobic pocket under the P-loop in these enzyme–ligand complexes, and the substitution groups at the 5-position of thiophene in **Compd. 3–5** were buried in this pocket with the phenyl headgroup and thiophene ring in close proximity to this pocket. Thus, hydrophobic interactions with the hydrophobic surface of this pocket are postulated to be dominant factors that contribute to the higher potencies of **Compd. 3**> and **Compd. 5** *vs.* **Compd. 4** (Fig. 2e and i *vs.* g).

Compd. 5 exhibited the highest inhibitory activity among **Compd. 1–5**. Thus, **Compd. 5** was used in 10 ns molecular dynamics (MD) simulations to validate the accuracy of the docking and calculate ΔG_{bind}. The root mean square deviation (RMSD) plot revealed that **Compd. 5** reached equilibrium after 2 ns (RMSD = 3.35 ± 0.48 Å; Fig. 3a), and the initial and final structures were similar (Fig. 3b), which indicated that the binding pocket and the conformation of the ligand were stable and the docking results were reliable.

After the MD simulations, we extracted the 7–8 ns period of the **Compd. 5**–S6K1 complex to calculate the ΔG_{bind} by using the MM/GBSA method.[11] The individual energy terms including the van der Waals contribution (ΔG_{vdw}), electrostatic contribution (ΔG_{ele}), polar contribution to solvation free energy (ΔG_{GB}) and non-polar contribution to solvation free energy (ΔG_{SA}) were also calculated. ΔG_{vdw}, ΔG_{SA}, ΔG_{ele}, ΔG_{GB}, and ΔG_{bind} were −54.60 kcal mol^{-1}, −6.08 kcal mol^{-1}, −26.74 kcal mol^{-1}, 43.31 kcal mol^{-1} and −44.12 kcal mol^{-1}, respectively (Table 1). We concluded that polar contributions (ΔG_{ele} + ΔG_{GB}) were less important than non-polar contributions (ΔG_{vdw} + ΔG_{SA}) to the S6K1 inhibitory activity of **Compd. 5**, and van der Waals interactions were crucial to the binding free energy of the inhibitor.

Table 1 The binding free energies for the S6K1–**Compd. 5** complex[a]

	ΔG_{vdw}	ΔG_{SA}	ΔG_{ele}	ΔG_{GB}	ΔG_{bind}
Ave.	−54.60	−6.08	−26.74	43.31	−44.12
S.D.	1.19	0.12	2.10	2.03	1.32

[a] All energies are in kcal mol^{-1}.

The total ΔG_{bind} of the S6K1–**Compd. 5** complex was decomposed using the MM/GBSA method to yield the individual energy contributions.[11] The contributions of the residues are presented in Fig. 2j and are −2.9527 kcal mol^{-1}, −2.1242 kcal mol^{-1}, −2.1029 kcal mol^{-1}, −1.8915 kcal mol^{-1}, −1.8517 kcal mol^{-1}, −1.3419 kcal mol^{-1}, −0.8753 kcal mol^{-1} and −0.2025 kcal mol^{-1} for Glu173, Val105, Leu175, Leu97, Met225, Glu222, Ala121 and Leu172, respectively (Fig. 4). We concluded that Leu97, Glu173, Leu175 and Met225 located in the hinge region and Val105 located in the hydrophobic pocket have important energy contributions (more than −1.85 kcal mol^{-1}). Additionally, Glu222, Ala121 and Leu172 showed positive contributions to the binding.

We previously developed potent and highly selective Rho kinase inhibitors with a pyrazole-phenyl scaffold and realized that hydrophobic benzodioxane and chroman groups bound within the hydrophobic pocket.[12,13] The optimization of **Compd. 5** started by replacing the central thiazole ring with a benzodioxane group or a chroman group while at the same time the indazole headgroup was lengthened to a pyrazole phenyl group. Since fluorine substituents affect nearly all adsorption, distribution, metabolism and excretion properties of a lead compound, fluorine substituents have become widespread and important drug components. After focusing previously on the design of bioactive fluorine-containing compounds,[14,15] we estimated that F substituents should contribute to enzyme inhibition and were introduced in this work. Three phenylpyrazole-based amides (**D1–D3**) with fluorine in the middle phenyl ring were designed as S6K1 inhibitors (Scheme 1). As expected, **D1–D3** interacted with Glu173 and Leu175 through H-bonds and with Val 105, Leu97, Met225 and Ala121 through hydrophobic interactions (Fig. 5). Molecular docking results indicated that the F

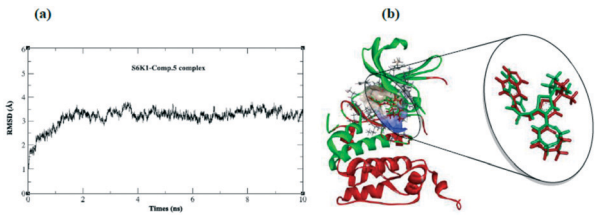

Fig. 3 MD simulation results. (a) Plot of RMSD *versus* time. (b) S6K1–**Compd. 5** complex. The initial and final structures are shown in red and green, respectively.

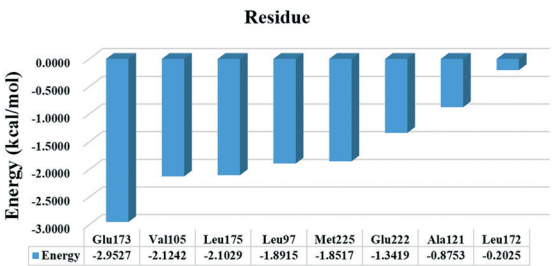

Fig. 4 Energy contributions of key residues.

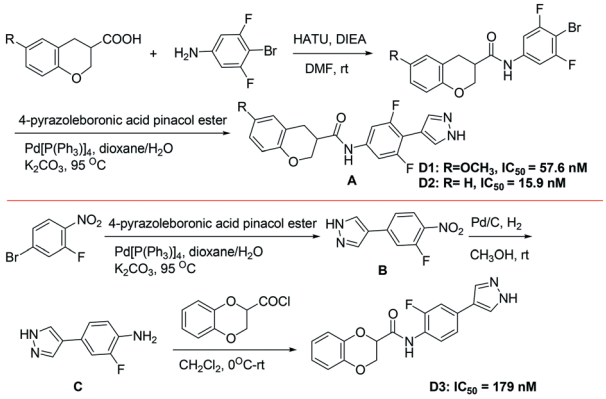

Scheme 1 Synthesis of **D1–D3**.

substituent at the third position of the middle phenyl ring formed a H-bond with Met225 (Fig. 5b, d, and f), and a H-bond interaction at the 2-position with an F substituent would decrease the activity of the inhibitor by distorting the inhibitor and forcing the benzodioxane ring away from the hydrophobic pocket (Fig. 5e).

Encouraged by the docking results for inhibitors **D1–D3**, the synthesis of these newly designed compounds was carried out (Scheme 1). **D1** and **D2** were readily synthesized by a short sequence that began with amide condensation of commercially available aniline and a chroman carboxylic acid to yield amide **A**. The pyrazole was then incorporated through standard palladium-catalyzed Suzuki coupling to give the desired products **D1** and **D2**. Similarly, a short sequence involving sequential Suzuki coupling between the 4-pyrazoleboronic acid pinacol ester and 4-bromo-2-fluoro-1-nitrobenzene, Pd/C catalyzed nitro reduction and the amide condensation reaction gave the inhibitor **D3**.

D1–D3 were then shipped to the Reaction Biology Corporation in the USA for biological activity testing. **D1–D3** exhibited similar inhibitory activity against S6K1 to **Compd. 3–5** (IC_{50} = 56.7 nmol L^{-1} for **D1**, 15.9 nmol L^{-1} for **D2**, and 179 nmol L^{-1} for **D3**), which indicated that the information obtained from the computational efforts successfully guided the design of potent S6K1 inhibitors.

The pharmacokinetic (PK) properties of **D1** and **D2** in Sprague-Dawley rats were studied (Table 2). **D1** demonstrated 28 mL min^{-1} kg^{-1} clearance (Cl), 0.7 L kg^{-1} volume of distribution (Vd), 1.6 μM h AUC, 0.67 nM oral Cmax and 25% bioavailability (%*F*), whereas **D2** demonstrated 29 mL min^{-1} kg^{-1} Cl, 0.8 L kg^{-1} Vd, 1.5 μM h AUC, 0.60 nM oral Cmax and 23% bioavailability.

Metabolism stabilities in liver microsomes of **D1** and **D2** were examined (Table 3). Neither **D1** nor **D2** showed high microsome stability. Half-lives ($t_{1/2}$) in humans were 23 and 37 min for **D1** and **D2**, respectively, whereas $t_{1/2}$ values in rats were 17 and 15 min for **D1** and **D2**, respectively.

To understand the reason for the short $t_{1/2}$ values of **D1** and **D2**, P450 inhibition of four major isoforms was evaluated using a cocktail inhibition assay. Percent inhibition (% inh.) of cytochrome P450 isoforms 1A2/2C9/2D6/3A4 at 10 μM were 42/63/40/38 for **D1** and 12/84/61/43 for **D2**, which indicated that 2C9 was the main CYP isoform causing the metabolism instabilities.

Experimental

Chemistry

All reagents and solvents were from commercially available sources and used without further purification unless otherwise stated. Thin layer chromatography (TLC) analysis was performed with a precoated silica gel. Column chromatography was carried out on silica gel (200–300 mesh). NMR spectra were recorded with a Bruker 500 MHz spectrometer. The line positions of multiplets were given in ppm (δ), and the coupling constants (J) were given in hertz. Elemental analysis was performed on a Thermo Fisher elemental analyzer. HRMS was performed with Solaril X70 FT-MS apparatus.

Synthesis of D1–D3

4-Bromo-3,5-difluoroaniline (1 mmol) was added to a stirred solution of a carboxylic acid derivative (1 mmol), HATU (1 mmol), and DIEA (3 mmol) in DMF at room temperature. After the amide coupling was finished, detected by TLC, DMF was removed under reduced pressure, and the obtained residue was extracted with EtOAc (3 × 20 mL). The combined organic phases were then washed with saturated brine (3 × 5 mL), dried over Na_2SO_4, and evaporated in a rotavap to give intermediate **A**, which was used without further purification.

$Pd[P(Ph)_3]_4$ (0.15 mmol) was added to a degassed mixture of 4-pyrazoleboronic acid pinacol ester (1.2 mmol), K_2CO_3 (3 mmol), and intermediate **A** (1 mmol) in dioxane/H_2O (2 mL, 4 : 1 by volume) under nitrogen protection. This solution was stirred at 95 °C until the complete disappearance of **A**. Then, the reaction mixture was concentrated under reduce pressure, extracted with EtOAc (3 × 20 mL), washed with brine (3 × 5 mL), dried over anhydrous Na_2SO_4, and evaporated in a rotavap to give a residue. Finally, the obtained residue was purified through flash column chromatography to give the targeted inhibitors **D1** and **D2**.

N-(3,5-Difluoro-4-(1*H*-pyrazol-4-yl)phenyl)-6-methoxychromane-3-carboxamide (**D1**): (58% yield over two steps). ^{1}H NMR (DMSO-d_6, 500 MHz) δ: 12.61 (br, 1H), 8.21 (br, 1H), 8.13–8.10 (m, 2H), 7.74–7.68 (m, 2H), 6.74–6.67 (m, 3H), 4.42–4.39 (m, 1H), 4.09–4.04 (m, 1H), 3.69 (s, 3H), 3.09–2.96 (m, 3H). ^{13}C NMR (DMSO-d_6, 125 MHz) δ: 159.95, 154.26, 152.11, 143.55, 142.78, 130.36, 130.05, 128.11, 119.77, 118.71, 114.53, 113.57, 112.22, 111.33, 58.75, 55.18, 52.19, 12.57. Anal. calcd for $C_{20}H_{17}F_2N_3O_3$: C, 62.33; H, 4.45; N, 10.90. Found: C, 62.32; H, 4.46; N, 10.91. HRMS calcd for $C_{20}H_{18}F_2N_3O_3$ [M + H^+]: 386.1316, found 386.1314.

N-(3,5-Difluoro-4-(1*H*-pyrazol-4-yl)phenyl)chromane-3-carboxamide (**D2**): (54% yield over two steps). ^{1}H-NMR (DMSO-d_6, 500 MHz) δ 8.46–8.44 (m, 1H), 8.10–8.09 (m, 2H),

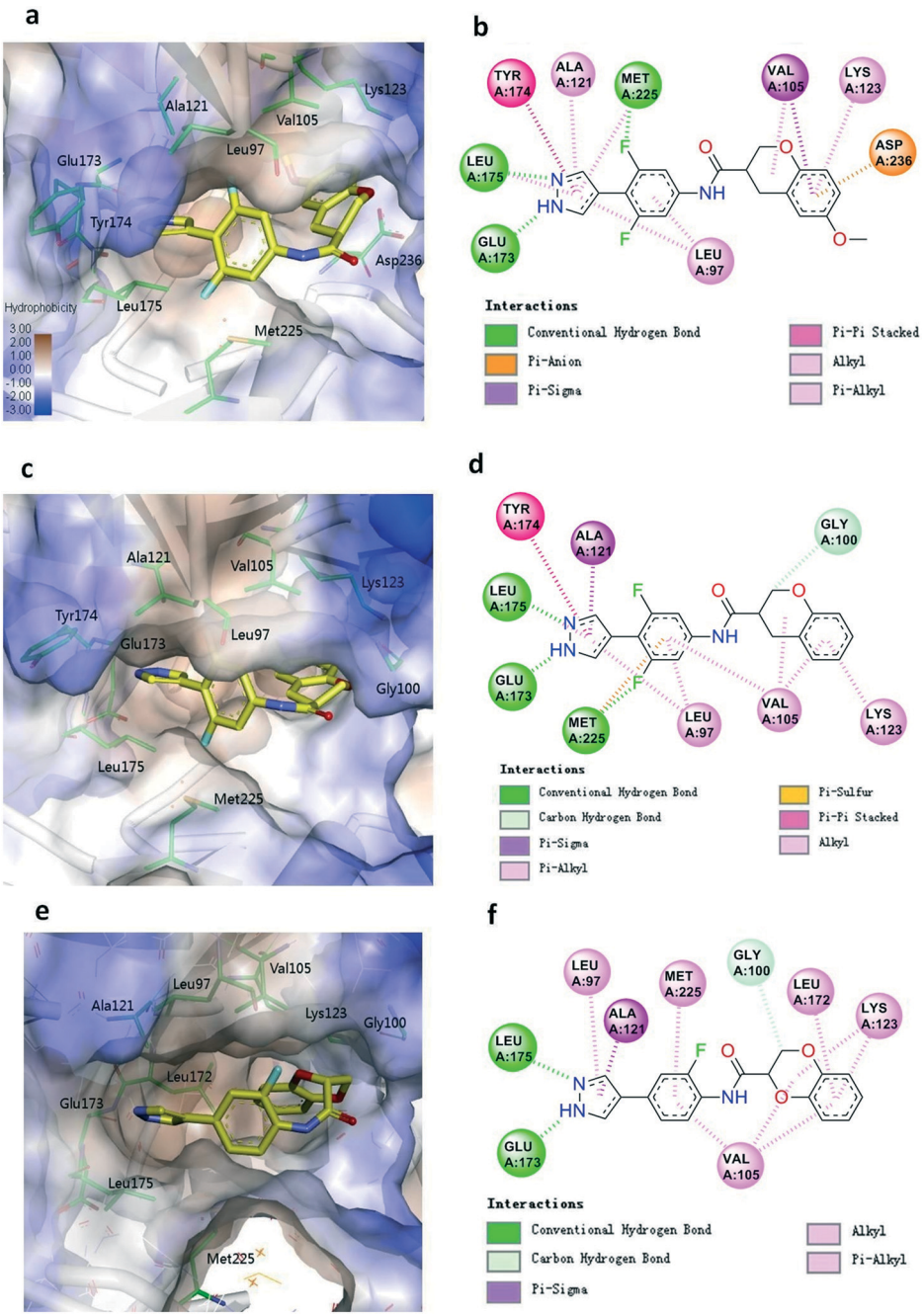

Fig. 5 Docking results of **D1**–**D3**. (a) 3D view of the S6K1–**D1** complex. (b) 2D view of the S6K1–**D1** complex. (c) 3D view of the S6K1–**D2** complex. (d) 2D view of the S6K1–**D2** complex. (e) 3D view of the S6K1–**D3** complex. (f) 2D view of the S6K1–**D3** complex. In the 3D view, carbon atoms in the ligand and protein are shown in yellow and white, respectively. In the 2D view, conventional hydrogen bonds and carbon H-bonds are shown as green dotted lines. Pi–sulfur, alkyl, pi–alkyl, pi–anion, pi–pi stacked and pi–sigma interactions are hydrophobic interactions. Pi–sulfur and pi–anion interactions are shown as yellow dotted lines, alkyl and pi–alkyl interactions are shown as pink dotted lines, and pi–sigma and pi–pi stacking are shown as purple dotted lines.

7.90–7.87 (m, 1H), 7.20–7.18 (m, 1H), 7.13–7.09 (m, 1H), 6.91–6.88 (m, 1H), 6.87–6.80 (m, 1H), 4.60–4.57 (m, 1H), 4.37–4.33 (m, 1H), 3.93–3.38 (m, 1H), 3.32–3.21 (m, 2H). ^{13}C NMR (DMSO-d_6, 125 MHz) δ: 159.34, 154.39, 152.13, 146.36, 142.72, 138.65, 130.14, 130.06, 128.01, 118.83, 116.20, 115.98, 114.55, 111.24, 58.70, 52.33, 12.57. Anal. calcd for $C_{19}H_{15}F_2N_3O_2$: C, 64.22; H, 4.26; N, 11.83. Found: C, 64.20; H, 4.25; N, 11.81. HRMS calcd for $C_{19}H_{16}F_2N_3O_2$ [M + H$^+$]: 356.1211, found 356.1214.

Following the procedure of **D1** and **D2** from intermediate **A**, intermediate **B** was obtained as a white solid from 4-bromo-2-fluoro-1-nitrobenzene. Then, a mixture of intermediate **B** (1 mmol), 5% Pd/C, and H_2 in CH_3OH (10 mL) was stirred at room temperature until the complete

Table 2 Rat pharmacological data for **D1** and **D2**[a]

Compd.	D1	D2
Cl (mL min^{-1} kg^{-1})	28 ± 5	29 ± 6
Vd (L K^{-1})	0.7 ± 0.2	0.8 ± 0.2
$t_{1/2}$ (h)	0.47 ± 0.1	0.5 ± 0.1
AUC (μM h)	1.6 ± 0.3	1.5 ± 0.2
Cmax (μM)	0.67 ± 0.03	0.6 ± 0.04
F (%)	25 ± 5	23 ± 5

[a] Data were the means of three determinations.

Table 3 Metabolism stabilities of **D1** and **D2**[a]

Compd.	% inh. at 10 μM 1A2/2C9/2D6/3A4	$t_{1/2}$ (min) Human	Rat
D1	42/63/40/38	23	17
D2	12/84/61/43	37	15

[a] Data were the means of three experiments with errors within 30% of the mean.

conversion of intermediate **B** detected by ^{1}H NMR. Then, the reaction mixture was filtered and concentrated to give aniline **C**.

$COCl_2$ (1.5 mmol) was added to a mixture of 2,3-dihydrobenzo[1,4]dioxine-2-carboxylic acid (1.1 mmol) in dry CH_2Cl_2 (5 mL) at 0 °C. Then, DMF (3–5 drops) was added to the mixture, and then the reaction mixture was stirred at room temperature for another 30 minutes and concentrated to dryness with a rotavap to give acid chloride as a white solid. To a solution of intermediate **C** (1 mmol) in dry CH_2Cl_2 (2 mL), acid chloride in dry CH_2Cl_2 (2 mL) and Et_3N (3 mmol) were added with nitrogen protection at 0 °C. After complete conversion of **C** detected by TLC, the reaction was quenched with saturated $NaHCO_3$ (2 mL) and extracted with EtOAc (3 × 20 mL). The combined organic phases were washed with brine (3 × 5 mL) again, dried over Na_2SO_4, concentrated under reduced pressure, and purified through flash column chromatography to give the targeted inhibitor **D3**.

N-(2-Fluoro-4-(1*H*-pyrazol-4-yl)phenyl)-2,3-dihydrobenzo[*b*]-[1,4]dioxine-2-carboxamide (**D3**): (50% yield over three steps). ^{1}H-NMR (DMSO-d_6, 500 MHz) δ 11.54 (br, NH, 1H), 8.43–8.40 (m, 2H), 8.04–8.03 (m, 1H), 7.90–7.89 (m, 1H), 7.61–7.59 (m, 1H), 7.13–7.11 (m, 1H), 6.88–6.87 (m, 2H), 6.63–6.62 (m, 1H), 5.12–5.11 (m, 1H), 4.46–4.42 (m, 1H), 4.34–4.31 (m, 1H). ^{13}C NMR (DMSO-d_6, 125 MHz) δ: 159.31, 158.76, 158.43, 154.89, 153.27, 144.01, 143.53, 141.72, 129.36, 128.57, 126.43, 121.74, 119.22, 117.87, 112.77, 112.05, 62.66, 54.94. Anal. calcd for $C_{18}H_{14}FN_3O_3$: C, 63.71; H, 4.16; N, 12.38. Found: C, 63.73; H, 4.15; N, 12.40. HRMS calcd for $C_{18}H_{15}FN_3O_3$ [M + H^+]:340.1097, found 340.1096.

S6K1 assay. S6K1 assay was carried out at the Reaction Biology Corporation and followed the protocols described on its web site. Compounds were tested in 10-dose IC_{50} mode with 2.5-fold serial dilution starting at 10 μM. Control compound staurosporine was tested in 10-dose IC_{50} mode with 3-fold serial dilution starting at 20 μM. Reactions were carried out at 5 μM ATP for S6K1 (Fig. 6).

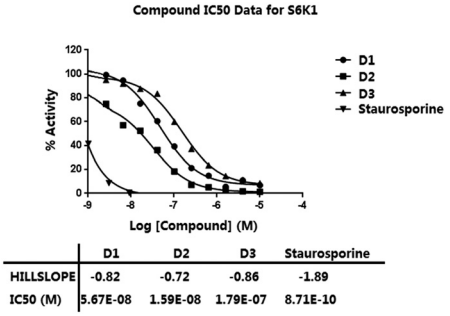

	D1	D2	D3	Staurosporine
HILLSLOPE	-0.82	-0.72	-0.86	-1.89
IC50 (M)	5.67E-08	1.59E-08	1.79E-07	8.71E-10

Fig. 6 Compounds' IC_{50} values against S6K1.

Pharmacokinetics.[16] Pharmacokinetic studies were conducted on Sprague Dawley rats. The compound was formulated in a generic formulation at 1 mg mL^{-1} and dosed at 1 mg kg^{-1} intravenously into the femoral vein or 2 mg kg^{-1} by oral gavage. Blood was obtained at t = 5 min, 15 min, 30 min, 1 h, 2 h, 4 h, 6 h, and 8 h. Blood was collected in EDTA containing tubes and plasma was generated by standard centrifugation methods. All procedures and handling were according to the standard operating procedures approved by the IACUC at Scripps Florida. All animal procedures were performed in accordance with the Guidelines for Care and Use of Laboratory Animals of The Scripps Research Institute at Scripps Florida and approved by the Animal Ethics Committee of The Scripps Research Institute.

In order to assess *in vivo* pharmacokinetic parameters, an LC-MS/MS bioanalytical method was developed where 25 μl of plasma was treated with 125 μl of acetonitrile containing an internal standard in a Millipore Multiscreen Solvinert 0.45 micron low binding PTFE hydrophilic filter plate (#MSRLN0450) and allowed to shake at room temperature for five minutes. The plate was then centrifuged for 5 minutes at 4000 rpm in a tabletop centrifuge and the filtrate was collected in a polypropylene capture plate. The filtrate (10 μl) is injected into an Agilent 1200 HPLC equipped with a Thermo Betasil C18 HPLC column 5 μ (50 × 2.1 mm) #70105-052130. Mobile phase A was water with 0.1% formic acid. Mobile phase B was acetonitrile with 0.1% formic acid. The flow rate was 375 μl min^{-1} using a gradient of 90% A/10% B from 0–0.5 min, ramped to 5% A/95% B at 2 min, held at 5% A/95% B until 3.0 min, ramped to 90% A/10% B at 4 min, and held at 90% A/10% B until 7 min.

An API Sciex 4000 equipped with a turbo ion spray source was used for all analytical measurements. MRM methods were carried out in positive ion mode. Peak areas of the analyte ions were measured against the peak areas of the internal standard. Data were fitted using WinNonLin using an IV bolus model.

P450 inhibition.[16] P450 inhibition of four major isoforms were evaluated using a cocktail inhibition assay, where the metabolism of specific marker substrates (CYP1A2, phenacetin demethylation to acetaminophen; CYP2C9,

tolbutamide hydroxylation to hydroxytolbutamide; CYP2D6, bufuralol hydroxylation to 4′-hydroxybufuralol; CYP3A4, midazolam hydroxylation to 1′-hydroxymidazolam) in the presence or absence of 10 μM probe compound was evaluated. The concentration of each marker substrate was approximately its Km. The conditions were similar to those described by Tesino and Patonay, except that 2C19 was not evaluated as we found that the stock solution of the 2C19 probe substrate, omeprazole, had poor stability. Specific inhibitors for each isoform were included in each run to validate the system.

Ligand preparation. The ligand preparation was performed using Sybyl-2.0. 3D structures of all compounds were constructed using the Sketch Molecule module and were minimized using the Tripos force field by the Powell gradient algorithm with Gasteiger–Hückel charges. The maximum iterations for the minimization were set to 10 000. The minimization was terminated when an energy gradient convergence criterion of 0.005 kcal mol^{-1} $Å^{-1}$ was reached.

Molecular docking.[10] Molecular docking was performed using the Surflex-Dock module in Sybyl (Tripos, USA). The crystal structure of human S6K1 for molecular docking was downloaded from the RCSB Protein Data Bank (http:/www.rcsb.org/pdb/home/home.do, PDB:3A60). The protein was prepared by using the biopolymer module implemented. All water molecules were removed, hydrogen atoms were added, the end residues were repaired, and energy minimization was performed on the protein. Docking calculations were performed through protomol generation using the ligand, the protein was fixed while the ligand was flexible, and the default parameters were used as described in the Sybyl manual unless otherwise specified. Subsequently, the ligand was docked into the ATP-binding site of S6K1 by an empirical scoring function. By default, each ligand generated 20 conformations, and the scores were forecasted based on the strength of the receptor–ligand interactions. The best docked conformation was selected for further studies.

MD simulations.[10,11] MD simulations were performed using AmberTools 14.0 package with the ff99SB force field for the kinase and the general AMBER force field (gaff) for the ligands. MD simulations followed the procedures of preparation, minimization, heating, density, balance, and production. In the beginning, the complex system was simulated in a TIP3P water box environment. In this process, the SHAKE algorithm was applied to restrain the stretching vibrations of all bonds involving hydrogen atoms, and the entire system suffered from energy minimization to eliminate possible space collisions with two steps: (1) the atom position of all solute species was restrained by a force of 100 kcal mol^{-1} $Å^{-2}$. The water molecules and ligands were minimized by 500 steps of the steepest descent method followed by 500 steps of the conjugated gradient method; (2) the entire system was energy optimized by 5000 steps of the steepest descent method followed by 5000 steps of the conjugated gradient method. Then, the system was heated from 0 to 300 K, followed by equilibration at 300 K over 50 ps. Finally, a 10 ns production run was carried out by the NPT ensemble at 300 K and 1.013×10^5 kPa. RMSD calculations of the equilibrated system and cluster analysis were carried out for selected compounds.

At length, a production run of 10 ns under conditions of constant pressure and temperature was carried out, and the MD trajectories of all systems were taken to calculate the binding free energy with the MM/GBSA method. To increase the accuracy of the binding free energy calculations, all energy components were calculated using 50 snapshots extracted from 7 to 8 ns based on the RMSD results. Finally, MM/GBSA free energy decomposition was run using SANDER in MMPBSA.py to obtain the quantitative information about the interactions between the inhibitors and the residues.

Conclusions

Based on five thiophene urea-based S6K1 inhibitors, molecular docking demonstrated that H-bonding interactions to residues Glu173 and Leu175 and hydrophobic interactions to residues Val105, Leu97 and Met225 were key elements for S6K1 inhibitory activities. 10 ns MD simulations supported the docking results. Binding free energy decomposition also indicated that Glu173, Val105, Leu175, Leu97 and Met225 contributed significantly to the binding free energy. S6K1 inhibitors **D1–D3** were then designed according to the computational results. The inhibitory activities of **D1–D3** obtained after synthesis and biological evaluation by S6K1 assay were as good as the lead compounds **Compd. 3–5**, which indicated that the molecular models were used effectively to design highly potent S6K1 inhibitors. Only medium bioavailabilities and microsome stabilities were observed. Future efforts with these compounds will focus on biological evaluations in cell lines and improving their metabolism stabilities.

Conflicts of interest

There are no conflicts to declare.

Acknowledgements

The authors acknowledge financial support from the National Natural Science Foundation of China (Grant No. 21502117), the Shanghai Gaofeng & Gaoyuan Project for University Academic Program Development, and the Shanghai Key Laboratory of Chemical Assessment and Sustainability (19DZ2271500). We are also grateful to Prof. Guanjun Wang for his support. Experimental help for Tables 2 and 3 from Lin Li and modification–polish of the resubmitted manuscript from the Edanz Group (https://en-author-services.edanzgroup.com/) are also greatly appreciated.

References

1 S. Metayer-Coustard, H. Mameri, I. Seiliez, S. Crochet, P. Crepieux, Y. Mercier, P. A. Geraert and S. Tesseraud, *J. Nutr.*, 2010, **140**, 1539–1545.

2 I. V. Zaiets, A. S. Sivchenko, A. I. Khoruzhenko, L. O. Savinska and V. V. Filonenko, *Ukr. Biochem. J.*, 2018, **90**, 25–35.
3 M. A. Smith, L. Katsouri, E. E. Irvine, M. K. Hankir, S. M. A. Pedroni, P. J. Voshol, M. W. Gordon, A. I. Choudhury, A. Woods and A. Vidal-Puig, *Cell Rep.*, 2015, **11**, 335–343.
4 M. M. Cao, Z. R. Zhang, S. Han and X. Lu, *Mol. Med. Rep.*, 2019, **19**, 3941–3947.
5 C. Selman, J. M. A. Tuller, D. Wieser, E. Irvine, S. J. Lingard, A. I. Choudhury, M. Claret, H. Al-Qassab, D. Carmignac, F. Ramadani, A. Woods, I. C. A. Robinson, E. Schuster, R. Batterham, S. C. Kozma, G. Thomas, D. Carling, K. Okkenhaug, J. M. Thornton, L. Partridge, D. Gems and D. J. Withers, *Science*, 2009, **326**, 140–144.
6 M. Fraenkel, M. Ketzinel-Gilad, Y. Ariav, O. Pappo, M. Karaca, J. Castel, M. F. Berthault, C. Magnan, E. Cerasi and N. Kaiser, *Diabetes*, 2008, **57**, 945–957.
7 S. H. Zhang, Z. M. Deng, C. Yao, P. Huang, Y. Zhang, S. B. Cao and X. C. Li, *PLoS One*, 2017, **12**, e0169585.
8 (*a*) J. Qin, R. Rajaratnam, L. Feng, J. Salami, J. S. Barber-Rotenberg, J. Domsic, P. Reyes-Uribe, H. Y. Liu, W. W. Dang and S. L. Berger, *J. Med. Chem.*, 2015, **58**, 305–314; (*b*) H. Zhang, M. L. Xiang, J. Y. Liang, T. Zeng, X. N. Zhang, J. Zhang and S. Y. Yang, *Mol. Diversity*, 2013, **17**, 767–772; (*c*) B. Bilanges and B. Vanhaesebroeck, *Biochem. J.*, 2010, **431**, e1–e3; (*d*) X. L. Xu, J. Sun, X. L. Xu, J. Sun, X. L. Xu, D. E. Doscas, X. L. Xu, X. N. Jiao, R. L. Song and A. J. Williamson, *Oncotarget*, 2017, **8**, 30438–30454; (*e*) C. Sylvain, I. M. Westwood, A. Kalusa, C. Cano, J. Travers, K. Boxall, C. L. Chow, S. Burns, J. Schmitt and L. Pickard, *Oncotarget*, 2013, **4**, 1647–1661.
9 P. Ye, C. Kuhn, M. Juan, R. Sharma, B. Connolly, G. Alton, H. Liu, R. Stanton and N. M. Kablaoui, *Bioorg. Med. Chem. Lett.*, 2011, **21**, 849–852.
10 (*a*) J. P. Pan, Y. Yin, L. H. Zhao and Y. B. Feng, *Bioorg. Med. Chem.*, 2019, **27**, 1382–1390; (*b*) M. Ding, Y. Yin, F. H. Wu, J. X. Cui, H. Zhou, G. G. Sun, J. Jiang and Y. B. Feng, *Bioorg. Med. Chem.*, 2015, **23**, 2505–2517.
11 T. J. Hou, J. M. Wang, Y. Y. Li and W. Wang, *J. Chem. Inf. Model.*, 2011, **51**, 69–82.
12 Y. B. Feng, Y. Yin, A. Weiser, E. Griffin, M. D. Cameron, L. Lin, C. Ruiz, S. Schürer, T. Inoue, V. Rao, T. Schroter and P. LoGrasso, *J. Med. Chem.*, 2008, **51**, 6642–6645.
13 Y. T. Chen, T. D. Bannister, A. Weiser, E. Griffin, L. Lin, C. Ruiz, M. D. Cameron, S. Schürer, D. Duckett, T. Schroter, P. LoGrasso and Y. B. Feng, *Bioorg. Med. Chem. Lett.*, 2008, **18**, 6406–6409.
14 (*a*) J. X. Cui, Y. Yin, W. Deng, M. Ding, Z. H. Wang, Y. Jiang, H. Zhou, G. F. Sun and Y. B. Feng, *Bioorg. Med. Chem.*, 2015, **23**, 7464–7477.
15 Z. Zhao, J. X. Cui, Y. Yin, H. Zhang, Y. C. Liu, R. Zeng, C. Fang, Z. P. Kai, Z. H. Wang and F. Wu, *Chin. J. Chem.*, 2016, **34**, 801–808.
16 Y. B. Feng, Y. Yin, A. Weiser, E. Griffin, M. D. Cameron, L. Lin, C. Ruiz, S. Schürer, T. Inoue, V. Rao, T. Schroter and P. LoGrassp, *J. Med. Chem.*, 2008, **51**, 6642–6645.

